universe

MDPI

Article

Plasma Effects on the Shadow of a Rotating Black Hole in Asymptotically Safe Gravity

Mou Xu, Haoyue Cong, Lili Guan, Zhengrui Guo and Jianbo Lu *

Department of Physics, Liaoning Normal University, Dalian 116029, China
* Correspondence: lvjianbo819@163.com

Abstract

We investigate the shadow of a rotating black hole in the infrared limit of asymptotically safe gravity (ASG), focusing on how different plasma distributions affect photon propagation and shadow properties. Using the Hamilton–Jacobi formalism, we derive the photon equations of motion in plasma and calculate the shadow boundary for three different plasma distributions. Relative to the case without plasma, a homogeneous plasma increases the shadow size, whereas radially and angularly inhomogeneous plasma distributions reduce it. The inhomogeneous plasma models make the shadow more circular, whereas the effect of a homogeneous plasma on the shadow shape depends on the ASG parameter $\tilde{\xi}$. The angularly inhomogeneous plasma has a stronger effect on the shadow size, whereas the radially inhomogeneous plasma has a greater influence on the shadow shape. For fixed plasma parameters, increasing $\tilde{\xi}$ reduces the shadow size and increases its departure from circularity. Overall, plasma has a more pronounced effect on the shadow size than on its shape. Finally, we use the EHT observations of Sgr A* to constrain the $(\tilde{\xi}, K_r)$ parameter space for the radially inhomogeneous plasma model. Under the conditions adopted in this work, the EHT observations mainly disfavor regions where both $\tilde{\xi}$ and K_r take relatively large values.

Keywords: asymptotically safe gravity; rotating black hole; black hole shadow; plasma; Event Horizon Telescope

1. Introduction

General relativity (GR), the standard theory of gravity, has passed a wide range of experimental and observational tests [1,2]. Alternative gravitational theories [3,4] and cosmological models [5,6] have also been investigated in the context of gravitational physics and cosmic evolution. However, within the conventional framework of perturbative quantization, GR is nonrenormalizable [7,8]. Nevertheless, GR can be consistently treated as a low-energy effective field theory, while its ultraviolet (UV) completion remains a central issue in quantum gravity [9]. The asymptotic safety scenario proposed by Weinberg provides a possible route to a nonperturbatively renormalizable and UV-complete theory of gravity [10,11]. Subsequently, Reuter derived a nonperturbative evolution equation governing the gravitational renormalization group flow within the effective average action framework [12]. The central idea of asymptotic safety is that the dimensionless gravitational couplings run with the renormalization group scale and approach finite values corresponding to a non-Gaussian fixed point in the ultraviolet [13,14]. In recent years, asymptotic safety has been explored in a wide range of contexts, including cosmology, gravitational collapse, and black hole (BH) physics [15–21].

Check for updates

Academic Editors: Yungui Gong, Emmanuel N. Saridakis, Maurice H.P.M. van Putten and Lorenzo Iorio

Received: 2 October 2026
Revised: 1 November 2026
Accepted: 9 November 2026
Published: 11 November 2026

Copyright: © 2026 by the authors. Licensee MDPI, Basel, Switzerland. This article is an open access article distributed under the terms and conditions of the Creative Commons Attribution (CC BY) license.

Black holes provide a natural theoretical laboratory for investigating quantum corrections in asymptotically safe gravity (ASG) [22–24]. Early studies applied renormalization group improvement to BH spacetimes by introducing a running Newton coupling to probe quantum gravity effects [25,26]. Subsequent studies obtained static, spherically symmetric BH solutions and constructed rotating BH spacetimes within ASG [27,28]. Various ASG BHs have also been extensively studied in terms of accretion, gravitational lensing, quasinormal modes, and greybody factors [29–36]. In the infrared limit of ASG, Haroon et al. used an approximate form of the running Newton coupling to construct a rotating BH spacetime characterized by a new parameter [37]. For this rotating BH spacetime, the Lense–Thirring effect, iron-line profiles from accretion disks, accretion flows, and chaotic particle motion have also been investigated [37–42].

The physical properties of compact objects, including black holes and traversable wormholes, have attracted considerable attention [43–48]. Strong gravitational lensing provides an important means of investigating photon motion in the vicinity of black holes. Virbhadra and Ellis investigated strong gravitational lensing and relativistic images around a Schwarzschild black hole [49]; Bozza developed an analytical method for gravitational lensing in the strong deflection limit of static, spherically symmetric spacetimes [50]; and Tsukamoto further improved this method [51]. These studies have provided an important theoretical basis for understanding light propagation in strong gravitational fields. In addition, light rays passing near a BH are significantly deflected by its strong gravitational field, while some photons are captured by the BH, producing a dark region on the observer's sky known as the BH shadow [52–54]. The shadow boundary is closely associated with the critical photon trajectories that separate photon capture from escape, while the shadow size and shape are strongly influenced by the BH spacetime geometry [55–60]. Therefore, the size and shape of BH shadows can provide valuable information about the spacetime geometry in the strong field regime and enable tests of gravity theories [61–73]. Advances in very-long-baseline interferometry (VLBI) have enabled significant progress in observations of BH shadows [74,75]. In 2019, the Event Horizon Telescope (EHT) Collaboration presented the first image of M87*, revealing a bright ring-like emission structure [76–78]. Subsequently, in 2022, the EHT Collaboration presented the first horizon-scale images of Sgr A*, providing a new observational window into the strong field regime around the BH [79,80].

In realistic astrophysical environments, BHs are generally surrounded by plasma [81–83]. Plasma is a dispersive medium in which the refractive index depends on the plasma frequency and the photon frequency. Consequently, light propagation in plasma differs from that in the absence of plasma [56,84,85]. As a result, plasma can alter the BH shadow, whose size and shape depend on the plasma distribution [86–90]. Perlick et al. investigated the influence of plasma on BH shadows in static spherically symmetric spacetimes [84]. Perlick and Tsupko subsequently extended this analysis to Kerr spacetime and identified the condition under which the Hamilton–Jacobi equation for light rays is separable. They then analyzed photon motion and the resulting BH shadow under this condition [85]. In this work, we investigate photon motion and the shadow of a rotating black hole in the infrared limit of ASG in the presence of three separable plasma distributions. We compare the effects of these plasma distributions and the ASG correction parameter on the shadow size and shape through the shadow observables. For the radially inhomogeneous plasma model, we further discuss the estimation of $(\tilde{\xi}, K_r)$ by combining the shadow area and oblateness, and investigate constraints on these parameters using EHT observations of Sgr A*.

This paper is organized as follows. Section 2 presents the rotating BH spacetime in the infrared limit of ASG and determines the parameter space admitting BH solutions with event horizons. In Section 3, we investigate photon motion and the shadow boundary of rotating

ASG BHs in plasma. Using the Hamilton–Jacobi equation, we derive the equations of photon motion and consider three plasma distributions—homogeneous, radially inhomogeneous, and angularly inhomogeneous—to examine their effects on the BH shadow. In Section 4, the shadow area, shadow radius, oblateness, and distortion parameter are calculated, and we analyze how these shadow observables vary with the plasma distribution and the ASG correction parameter. For the radially inhomogeneous plasma, we further use the shadow area and oblateness to estimate the model parameters. The ASG correction parameter $\tilde{\xi}$ and the radially inhomogeneous plasma parameter K_r are constrained using EHT observations of the Sgr A* shadow in Section 5. Finally, Section 6 summarizes our conclusions. Unless otherwise stated, we adopt geometrized units with $G_N = c = \hbar = 1$.

2. Rotating Black Hole in the Infrared Limit of Asymptotically Safe Gravity

Following Ref. [37], we consider an RG-improved rotating BH spacetime in the infrared limit of ASG, in which Newton's constant G is replaced by a running Newton coupling $G(r)$ that depends on the radial coordinate r. At large radial distances, the renormalization group scale p is asymptotically related to the radial coordinate by $p \sim 1/r$, corresponding to the infrared limit [27,37]. In this limit, the running Newton coupling can be approximated as [37,91]:

$$G(r) \simeq G_N\left(1 - \frac{\xi}{r^2}\right), \tag{1}$$

where ξ is a parameter with dimensions of length squared that characterizes the quantum correction to the spacetime geometry [91]. As Equation (1) is an infrared approximation, its applicability requires the correction term ξ/r^2 to be sufficiently small. As pointed out in [37], this approximation is not valid at very small radial distances. Using this infrared form of the running Newton coupling, Ref. [37] obtained the corresponding RG-improved rotating BH metric, which in Boyer–Lindquist coordinates can be written as

$$\begin{aligned} ds^2 = &-\left(1 - \frac{2Mr}{\Sigma}\left(1 - \frac{\xi}{r^2}\right)\right)dt^2 - \frac{4aMr\sin^2\theta}{\Sigma}\left(1 - \frac{\xi}{r^2}\right)dtd\phi + \frac{\Sigma}{\Delta}dr^2 + \Sigma d\theta^2 \\ &+ \sin^2\theta\left[r^2 + a^2 + \frac{2a^2Mr}{\Sigma}\sin^2\theta\left(1 - \frac{\xi}{r^2}\right)\right]d\phi^2, \end{aligned} \tag{2}$$

where

$$\Sigma = r^2 + a^2\cos^2\theta, \qquad \Delta = r^2 - 2Mr + \frac{2M\xi}{r} + a^2. \tag{3}$$

Here, M and a denote the BH mass and spin parameter, respectively. Ref. [37] also derived the rotating metric given in Equation (2) from the corresponding static and spherically symmetric spacetime [27] using a modified Newman–Janis algorithm [92]. The metric in Equation (2) is constructed through RG improvement rather than by directly solving the full field equations of ASG. Reuter and Tuiran [28] discussed the interpretation of an effective source associated with RG-improved Kerr geometries as fictitious "pseudo matter" representing the corrections introduced by RG improvement. When $\xi = 0$, $G(r)$ reduces to Newton's constant G_N, and the rotating spacetime reduces to the Kerr spacetime.

The event horizon of the rotating BH is determined by $g^{rr} = 0$, or equivalently by $\Delta(r_{\rm H}) = 0$. According to Equation (3), the horizon radius $r_{\rm H}$ of the rotating ASG BH satisfies

$$r_{\rm H}^3 - 2Mr_{\rm H}^2 + a^2 r_{\rm H} + 2M\xi = 0. \tag{4}$$

When Equation (4) admits two distinct positive real roots, the smaller and larger roots correspond to the inner and outer horizons, respectively. To further analyze the parameter space, we introduce the dimensionless parameters:

$$\tilde{a} = \frac{a}{M}, \qquad \tilde{\xi} = \frac{\xi}{M^2}. \tag{5}$$

By analyzing Equation (4), we determine the BH region in the $(\tilde{a}, \tilde{\xi})$ parameter plane, as shown in Figure 1. The red solid curve represents the critical case in which the inner and outer horizons merge, separating the BH and naked singularity regions. The blue region corresponds to the BH parameter space, while the region above the critical curve represents the naked singularity region, where no horizons are present. As shown in Figure 1, the allowed range of $\tilde{\xi}$ for BH solutions gradually decreases as the spin parameter $\tilde{a}$ increases.

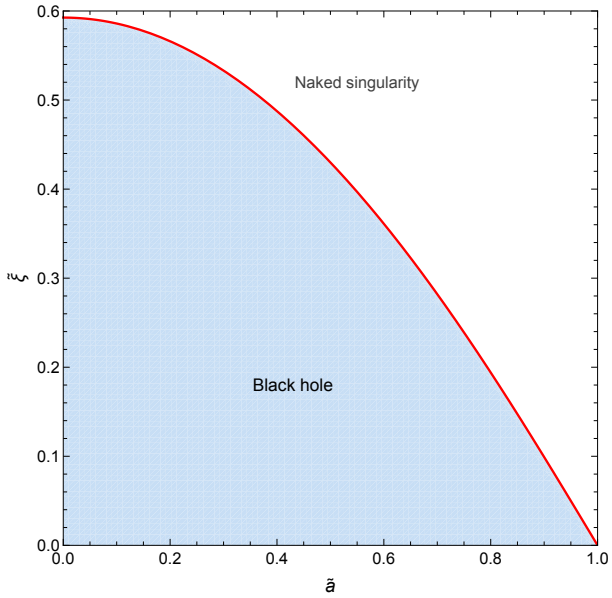


Figure 1. Parameter space of the rotating ASG solution, showing the black hole and naked singularity regions.

3. Photon Motion and Shadow of the Rotating ASG Black Hole in a Plasma Environment

Astrophysical BHs are generally surrounded by plasma [81,82], whose refractive and dispersive properties can modify the photon propagation in the vicinity of the BH and consequently affect the shadow boundary [85,86,93,94]. In this section, we investigate photon motion and the shadow of the rotating ASG BH in the presence of plasma. We employ the Hamilton–Jacobi formalism to study photon motion and consider plasma distributions that allow the Hamilton–Jacobi equation to be separable [85,86]. The shadow boundary is then determined by unstable spherical photon orbits. We further consider three plasma models with different distributions and compare their effects on the BH shadow boundary.

3.1. Photon Motion in Plasma

In the geometric optics approximation, photon motion in a nonmagnetized and pressureless plasma can be described by the Hamiltonian [85,86]:

$$\mathcal{H}(x,p) = \frac{1}{2}\left[g^{\mu\nu}(x)p_\mu p_\nu + \omega_p^2(x)\right] = 0, \tag{6}$$

where p_μ represents the canonical four-momentum of the photon, and ω_p is the plasma frequency, which is related to the electron number density N_e by [85]:

$$\omega_p^2 = \frac{4\pi e^2}{m_e} N_e, \tag{7}$$

with e and m_e denoting the electron charge and mass, respectively. The refractive index of the plasma satisfies [85]:

$$n^2 = 1 - \frac{\omega_p^2}{\omega^2}, \tag{8}$$

where ω is the photon frequency. Therefore, light can propagate through the plasma only when $\omega \geq \omega_p$. Since plasma is a dispersive medium, the black hole shadow can depend on the photon frequency [84].

For the stationary and axisymmetric spacetime described by Equation (2), if the plasma frequency ω_p is also independent of t and ϕ, photon motion has two conserved quantities [85]:

$$E = -p_t, \qquad L = p_\phi, \tag{9}$$

where E and L denote the conserved energy and azimuthal angular momentum of the photon, respectively. The conserved energy E corresponds to the photon frequency measured by a static observer at infinity. To obtain the equations of photon motion, we employ the Hamilton–Jacobi formalism [85], and the associated Hamilton–Jacobi equation takes the form:

$$\mathcal{H}\left(x, \frac{\partial S}{\partial x}\right) = 0. \tag{10}$$

To investigate the separability of the Hamilton–Jacobi equation, we assume the following separable form for the Jacobi action:

$$S = -Et + L\phi + S_r(r) + S_\theta(\theta). \tag{11}$$

Substituting Equation (11) into Equation (10) and using the metric in Equation (2), we obtain:

$$\begin{aligned} 0 = {} & (r^2 - 2Mr + \frac{2M\xi}{r} + a^2)\left(\frac{dS_r}{dr}\right)^2 - \frac{\left[(r^2+a^2)E - aL\right]^2}{r^2 - 2Mr + \frac{2M\xi}{r} + a^2} + \left(\frac{dS_\theta}{d\theta}\right)^2 \\ & + \left(aE\sin\theta - \frac{L}{\sin\theta}\right)^2 + \Sigma\omega_p^2. \end{aligned} \tag{12}$$

For the Hamilton–Jacobi equation to be separable, the plasma frequency must satisfy [85,86]:

$$\omega_p^2(r,\theta) = \frac{f_r(r) + f_\theta(\theta)}{\Sigma}, \tag{13}$$

where $f_r(r)$ and $f_\theta(\theta)$ are functions only of r and θ, respectively.

Under this separability condition, the Hamilton–Jacobi equation separates into radial and angular parts, yielding four first-order equations governing photon motion:

$$\Sigma\dot{t} = \frac{r^2 + a^2}{r^2 - 2Mr + \frac{2M\xi}{r} + a^2}\left[(r^2+a^2)E - aL\right] - a\left(aE\sin^2\theta - L\right), \tag{14}$$

$$\Sigma\dot{r} = \pm\sqrt{R(r)}, \tag{15}$$

$$\Sigma\dot{\theta} = \pm\sqrt{\Theta(\theta)}, \tag{16}$$

$$\Sigma\dot{\phi} = \frac{a}{r^2 - 2Mr + \frac{2M\xi}{r} + a^2}\left[(r^2+a^2)E - aL\right] - aE + \frac{L}{\sin^2\theta}, \tag{17}$$

where the overdot denotes differentiation with respect to the affine parameter [85,86]. The radial and angular functions are given by

$$R(r) = \left[(r^2+a^2)E - aL\right]^2 - (r^2 - 2Mr + \frac{2M\xi}{r} + a^2)\left[\mathcal{Q} + (L-aE)^2 + f_r(r)\right], \tag{18}$$

and

$$\Theta(\theta) = \mathcal{Q} + \cos^2\theta\left(a^2E^2 - \frac{L^2}{\sin^2\theta}\right) - f_\theta(\theta), \tag{19}$$

where $\mathcal{Q}$ is the generalized Carter constant associated with the separation of variables [85,95]. For convenience, we introduce the impact parameters:

$$\lambda = \frac{L}{E}, \qquad \eta = \frac{\mathcal{Q}}{E^2}, \tag{20}$$

and define $F_r(r) = \frac{f_r(r)}{E^2}$ and $F_\theta(\theta) = \frac{f_\theta(\theta)}{E^2}$. With these definitions, the radial function can be rewritten as

$$\mathcal{R}(r) = \left[(r^2+a^2) - a\lambda\right]^2 - (r^2 - 2Mr + \frac{2M\xi}{r} + a^2)\left[\eta + (\lambda-a)^2 + F_r(r)\right], \tag{21}$$

while the angular function becomes

$$\Theta(\theta) = \eta + \cos^2\theta\left(a^2 - \lambda^2\csc^2\theta\right) - F_\theta(\theta). \tag{22}$$

In addition, the allowed angular motion requires $\Theta(\theta) \geq 0$.

3.2. Spherical Photon Orbits

The BH shadow boundary is determined by critical photon trajectories associated with unstable spherical photon orbits [96,97]. For a spherical photon orbit located at $r = r_{\rm ph}$, the radial function satisfies [85]:

$$\mathcal{R}(r_{\rm ph}) = 0, \qquad \mathcal{R}'(r_{\rm ph}) = 0, \tag{23}$$

where the prime denotes differentiation with respect to the radial coordinate r. An unstable spherical photon orbit additionally satisfies

$$\mathcal{R}''(r_{\rm ph}) > 0. \tag{24}$$

The corresponding critical impact parameters for the rotating ASG BH are given by

$$\lambda(r_{\rm ph}) = \frac{r_{\rm ph}^2 + a^2}{a} - \frac{r_{\rm ph}^3 - 2Mr_{\rm ph}^2 + a^2 r_{\rm ph} + 2M\xi}{2a\left(r_{\rm ph}^3 - Mr_{\rm ph}^2 - M\xi\right)} \left[2r_{\rm ph}^2 + \sqrt{4r_{\rm ph}^4 - 2\left(r_{\rm ph}^3 - Mr_{\rm ph}^2 - M\xi\right)F_r'(r_{\rm ph})}\right], \tag{25}$$

and

$$\eta(r_{\rm ph}) = \frac{r_{\rm ph}\left(r_{\rm ph}^3 - 2Mr_{\rm ph}^2 + a^2 r_{\rm ph} + 2M\xi\right)}{4\left(r_{\rm ph}^3 - Mr_{\rm ph}^2 - M\xi\right)^2} \left[2r_{\rm ph}^2 + \sqrt{4r_{\rm ph}^4 - 2\left(r_{\rm ph}^3 - Mr_{\rm ph}^2 - M\xi\right)F_r'(r_{\rm ph})}\right]^2 - \left[\lambda(r_{\rm ph}) - a\right]^2 - F_r(r_{\rm ph}). \tag{26}$$

To project the critical impact parameters onto the observer's celestial coordinates, we consider an observer located at infinity with an inclination angle θ_o. The celestial coordinates are defined as [86,98]

$$X = \lim_{r_o\to\infty}\left(-r_o^2\sin\theta_o, \frac{d\phi}{dr}\right)|_{(r_o,\theta_o)}, \tag{27}$$

and

$$Y = \lim_{r_o \to \infty} \left(r_o^2, \frac{d\theta}{dr} \right) |_{(r_o, \theta_o)} . \tag{28}$$

For a given plasma model, the BH shadow boundary is obtained by substituting the critical impact parameters $\lambda(r_{\rm ph})$ and $\eta(r_{\rm ph})$ into the celestial coordinates over the allowed range of $r_{\rm ph}$.

3.3. Shadow Cast in Different Plasma Distributions

To compare the effects of different plasma distributions on the BH shadow, we consider three plasma models that satisfy the separability condition of the Hamilton–Jacobi equation: homogeneous, radially inhomogeneous, and angularly inhomogeneous plasmas.

(I) Homogeneous plasma.

We first consider a homogeneous plasma model in which the plasma frequency is independent of spatial position [85]. For $\omega_p = \text{const.}$, Equation (13) gives

$$F_r(r) = K_0 r^2, \qquad F_\theta(\theta) = K_0 a^2 \cos^2\theta, \tag{29}$$

where K_0 is the homogeneous plasma parameter, with $0 \leq K_0 < 1$. For an equatorial observer, the corresponding celestial coordinates are

$$X = -\frac{\lambda}{\sqrt{1 - K_0}}, \qquad Y = \pm\sqrt{\frac{\eta}{1 - K_0}}. \tag{30}$$

(II) Radially inhomogeneous plasma.

In the Shapiro accretion model, the plasma density decreases with the radial coordinate as $r^{-3/2}$ [99]. To satisfy the separability condition of the Hamilton–Jacobi equation, we adopt a separable, Shapiro-type radially inhomogeneous plasma distribution [85,86]:

$$F_r(r) = K_r \sqrt{M^3 r}, \qquad F_\theta(\theta) = 0, \tag{31}$$

where K_r is the radially inhomogeneous plasma parameter. For an equatorial observer, the corresponding celestial coordinates are

$$X = -\lambda, \qquad Y = \pm\sqrt{\eta}. \tag{32}$$

(III) Angularly inhomogeneous plasma.

Finally, we consider a plasma distribution with angular dependence [85]:

$$F_r(r) = 0, \qquad F_\theta(\theta) = K_\theta M^2 \left(1 + 2\sin^2\theta\right), \tag{33}$$

where K_θ is the angularly inhomogeneous plasma parameter. For an equatorial observer, the corresponding celestial coordinates are

$$X = -\lambda, \qquad Y = \pm\sqrt{\eta - 3K_\theta M^2}. \tag{34}$$

For the plasma distributions considered in this work, the parameters K_0, K_r, and K_θ are defined through the energy-normalized functions $F_r = f_r/E^2$ and $F_\theta = f_\theta/E^2$. Since E is proportional to the photon frequency measured by a distant observer, these parameters encode the frequency dependence of the plasma effects. Based on the above critical impact parameters and the corresponding celestial coordinates for different plasma distributions, we obtain the shadow cast by the rotating ASG BH for various parameters, as shown in Figure 2. In the numerical calculations, the spin parameter is fixed at $\tilde{a} = 0.5$, and we consider an equatorial observer with $\theta_o = \pi/2$. Figure 2a shows how the shadow changes with $\tilde{\xi}$ for

fixed $K_r = 2$. As $\tilde{\xi}$ increases, the shadow size gradually decreases, whereas the change in its shape is comparatively small, indicating that, within the parameter range considered, $\tilde{\xi}$ has a more pronounced effect on the shadow size than on its shape. To examine the effects of different plasma distributions, we fix $\tilde{\xi} = 0.1$, and Figure 2b–d shows the shadows cast by the BH in homogeneous, radially inhomogeneous, and angularly inhomogeneous plasmas, respectively. In this work, we choose illustrative values of the plasma parameters to examine the effects of different plasma distributions and their strengths on the size and shape of the black hole shadow. In the presence of homogeneous plasma, the shadow becomes larger as K_0 increases. By contrast, the shadow becomes smaller with increasing K_r and K_θ for radially and angularly inhomogeneous plasmas, respectively. These results demonstrate that the impact of plasma on the shadow size depends on its distribution: homogeneous plasma enlarges the shadow, whereas radially and angularly inhomogeneous plasmas reduce it. The effects of radially and angularly inhomogeneous plasmas on the shadow size are qualitatively consistent with the effect of increasing $\tilde{\xi}$. Within the parameter range explored in this work, the ASG correction parameter and plasma parameters mainly affect the shadow size, while their influence on the shadow shape is relatively weak.

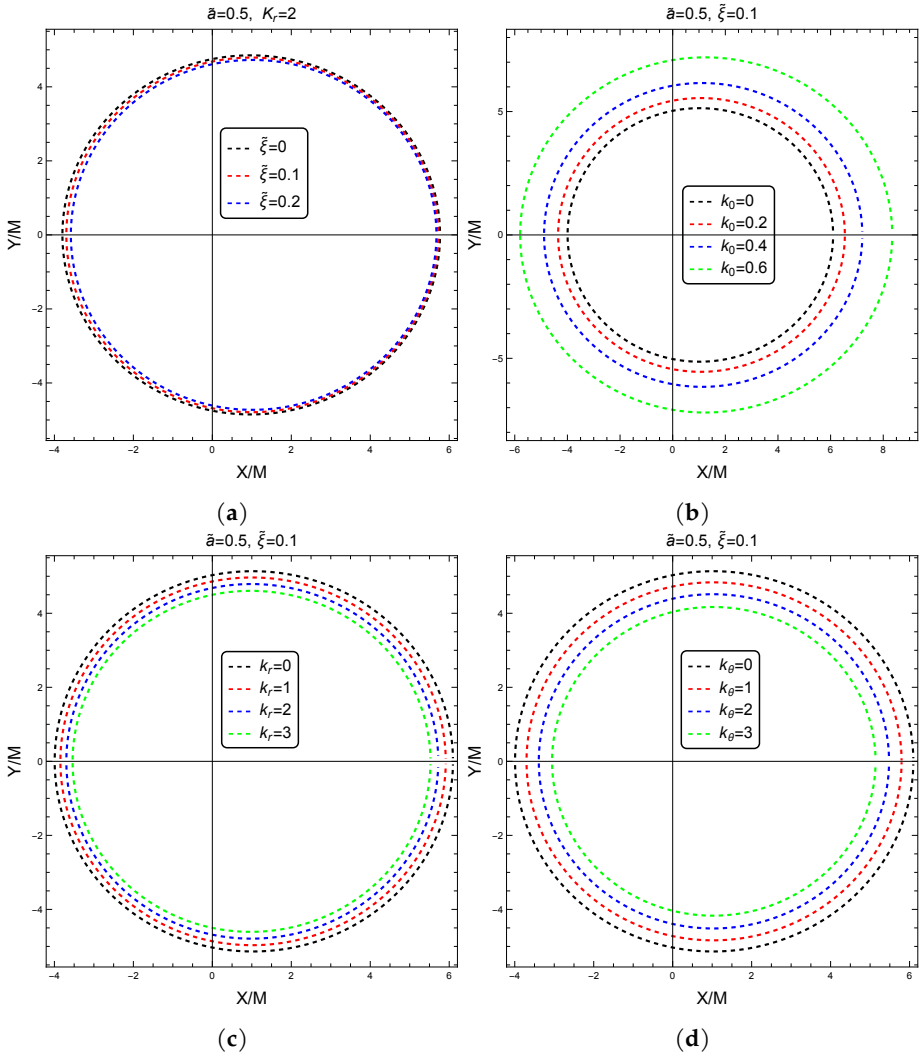


Figure 2. Shadows cast by the rotating ASG black hole for different plasma models and parameter values. The spin parameter is $\tilde{a} = 0.5$, and the observer is located in the equatorial plane, $\theta_o = \pi/2$. (**a**) Shadow for different values of $\tilde{\xi}$. (**b**) Homogeneous plasma. (**c**) Radially inhomogeneous plasma. (**d**) Angularly inhomogeneous plasma.

4. Shadow Observables and Parameter Estimation for the Rotating ASG Black Hole

In Section 3, we qualitatively analyzed the effects of the ASG correction parameter and different plasma distributions on the BH shadow. Building on this analysis, we quantitatively characterize the shadow size and shape using shadow observables and investigate how these observables are affected by different plasma distributions and the ASG correction parameter. We further use the shadow area and oblateness to estimate the ASG correction parameter and the plasma parameter.

4.1. Shadow Observables

To quantitatively characterize the size and shape of the BH shadow, we consider four shadow observables: the shadow area A, shadow radius R_s, oblateness D, and distortion parameter δ_s [100,101]. Among these quantities, A and R_s characterize the overall size of the shadow, whereas D and δ_s describe its shape. For the equatorial observer considered in this work, the shadow is symmetric with respect to the X axis. We denote the leftmost, rightmost, top, and bottom points of the shadow by $(X_l, 0)$, $(X_r, 0)$, (X_t, Y_t), and (X_b, Y_b), respectively. We first introduce a reference circle passing through the top, bottom, and rightmost points of the shadow, and define its radius R_s as the shadow radius [100]:

$$R_s = \frac{(X_t - X_r)^2 + Y_t^2}{2|X_r - X_t|}. \tag{35}$$

The center of the reference circle is located at $(X_c, 0)$, where

$$X_c = \frac{X_t^2 + Y_t^2 - X_r^2}{2(X_t - X_r)}. \tag{36}$$

Accordingly, the leftmost point of the reference circle on the X axis is given by

$$X_l' = X_c - R_s. \tag{37}$$

The horizontal displacement between the leftmost point of the shadow and that of the reference circle characterizes the distortion of the shadow. The distortion parameter δ_s is therefore defined as [100]

$$\delta_s = \frac{|X_l' - X_l|}{R_s}. \tag{38}$$

For a circular shadow, $\delta_s = 0$, while a larger value of δ_s indicates a greater deviation in the shadow from the reference circle.

In addition to the shadow radius R_s and distortion parameter δ_s, the shadow size and shape can also be characterized by the area A and oblateness D, respectively. The shadow area A is defined as [101]

$$A = 2\int_{r_{\rm ph}^-}^{r_{\rm ph}^+} Y(r_{\rm ph}) \frac{dX(r_{\rm ph})}{dr_{\rm ph}} dr_{\rm ph}, \tag{39}$$

where $r_{\rm ph}^-$ and $r_{\rm ph}^+$ denote the radii of the prograde and retrograde circular photon orbits, respectively. The oblateness D of the shadow is defined as the ratio of its horizontal diameter to its vertical diameter [101]:

$$D = \frac{X_r - X_l}{Y_t - Y_b}. \tag{40}$$

For the equatorial observer considered in this work, the shadow is symmetric about the X axis, so that $Y_b = -Y_t$, and Equation (40) reduces to

$$D = \frac{X_r - X_l}{2Y_t}. \tag{41}$$

For a circular shadow, $D = 1$, while the deviation of D from unity reflects the difference between the horizontal and vertical extents of the shadow.

Based on the shadows cast by the rotating ASG BH in Section 3, we calculate the shadow radius R_s and shadow area A using Equations (35) and (39), respectively. Figures 3 and 4 show the variations of A/M^2 and R_s/M with the corresponding plasma parameters for a fixed spin parameter $\tilde{a} = 0.5$, where the black, red, and blue curves correspond to $\tilde{\xi} = 0,\ 0.1,\ 0.2$, respectively. When K_0, K_r, and K_θ are set to zero, the three plasma models all reduce to the cases without plasma. For the homogeneous plasma, both A/M^2 and R_s/M increase as K_0 increases. In contrast, for the radially and angularly inhomogeneous plasmas, both A/M^2 and R_s/M decrease monotonically with increasing K_r and K_θ, respectively. Moreover, within the parameter ranges considered in this work, the variations of A/M^2 and R_s/M with K_θ are larger than those with K_r, indicating that the angularly inhomogeneous plasma produces a stronger change in the shadow size. On the other hand, for fixed plasma parameters, both A/M^2 and R_s/M decrease with increasing $\tilde{\xi}$ in all three plasma models.

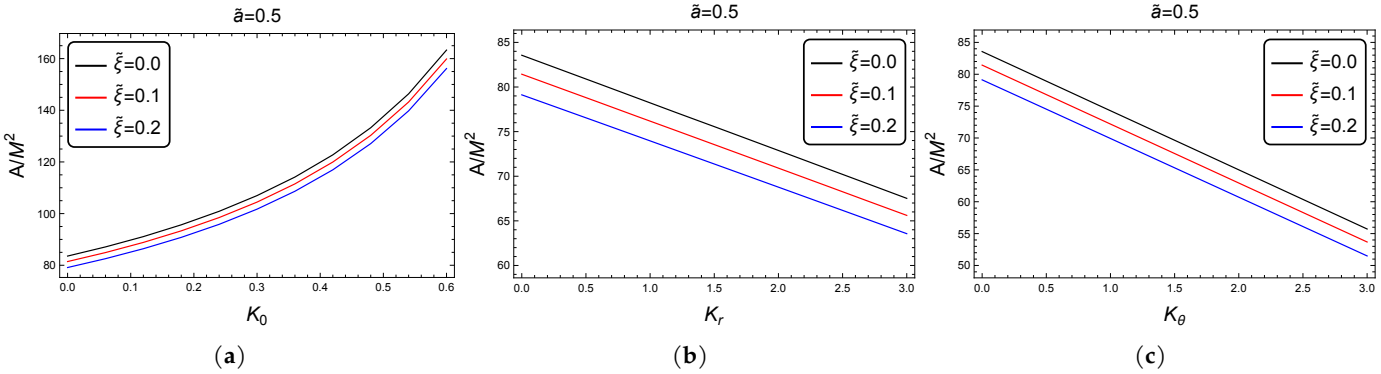


Figure 3. Variation in the shadow area A/M^2 of the rotating ASG black hole with the plasma parameter for different plasma models. The spin parameter is $\tilde{a} = 0.5$, and the black, red, and blue curves correspond to $\tilde{\xi} = 0,\ 0.1,\ 0.2$, respectively. (**a**) Homogeneous plasma. (**b**) Radially inhomogeneous plasma. (**c**) Angularly inhomogeneous plasma.

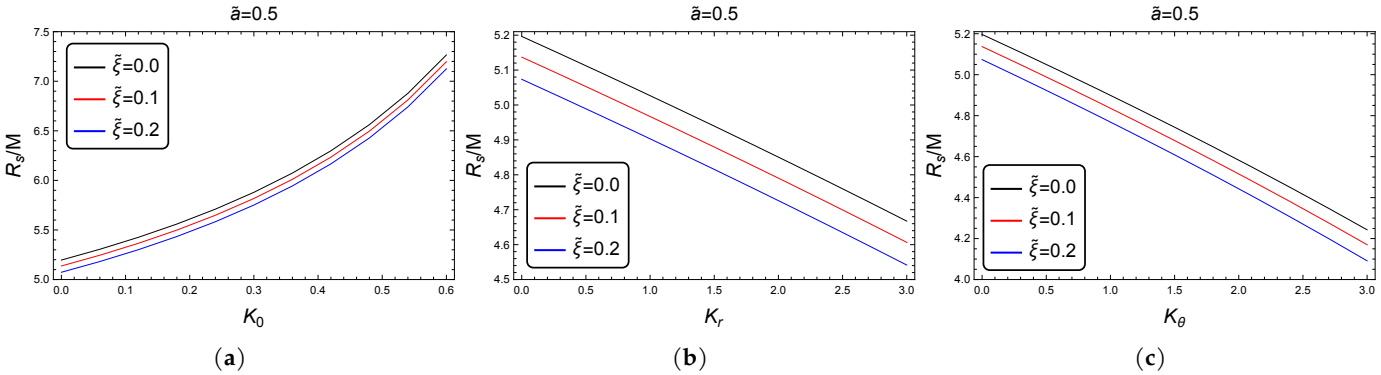


Figure 4. Variation in the shadow radius R_s/M of the rotating ASG black hole with the plasma parameter for different plasma models. The spin parameter is $\tilde{a} = 0.5$, and the black, red, and blue curves correspond to $\tilde{\xi} = 0,\ 0.1,\ 0.2$, respectively. (**a**) Homogeneous plasma. (**b**) Radially inhomogeneous plasma. (**c**) Angularly inhomogeneous plasma.

We further analyze the changes in the shadow shape using the oblateness D and distortion parameter δ_s, with the results shown in Figures 5 and 6, respectively. Within the parameter ranges considered in this work, for fixed plasma parameters, D generally decreases while δ_s increases as $\tilde{\xi}$ increases, indicating that the ASG correction increases the deviation in the shadow from circularity. For radially and angularly inhomogeneous plasmas, D generally increases while δ_s gradually decreases with increasing K_r and K_θ, respectively,

showing that both inhomogeneous plasma distributions make the shadow progressively more circular. A further comparison shows that the radially inhomogeneous plasma has a more pronounced effect on the shadow shape than the angularly inhomogeneous plasma and makes the shadow closer to circularity. Notably, the influence of the homogeneous plasma on the shadow shape depends on the ASG quantum correction. In the Kerr limit ($\tilde{\xi} = 0$), D decreases slightly while δ_s increases slightly as K_0 increases. By contrast, when $\tilde{\xi} = 0.2$, the trends are reversed, with D increasing and δ_s decreasing. This indicates that the ASG quantum correction can alter the way homogeneous plasma affects the shadow shape.

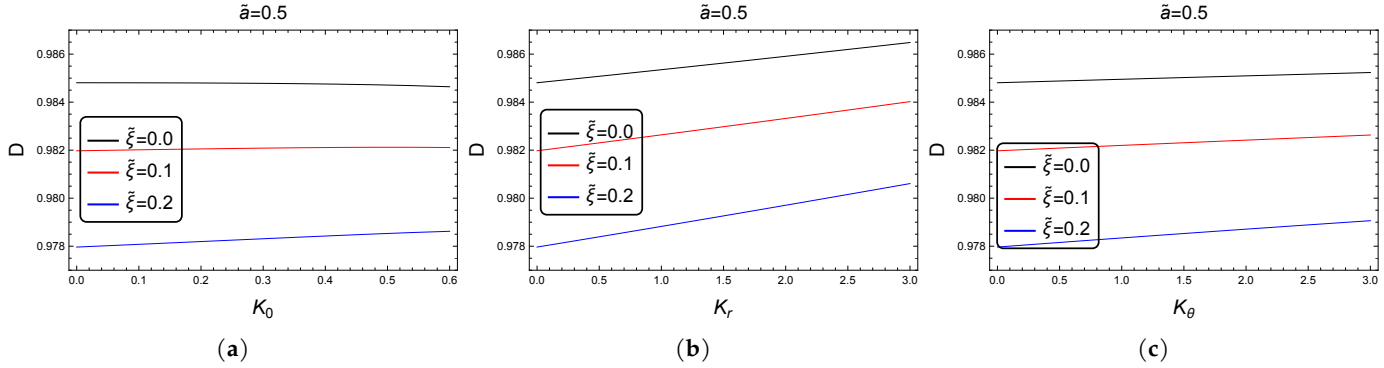


Figure 5. Variation in the oblateness D of the rotating ASG black hole with the plasma parameter for different plasma models. The spin parameter is $\tilde{a} = 0.5$, and the black, red, and blue curves correspond to $\tilde{\xi} = 0,\ 0.1,\ 0.2$, respectively. (**a**) Homogeneous plasma. (**b**) Radially inhomogeneous plasma. (**c**) Angularly inhomogeneous plasma.

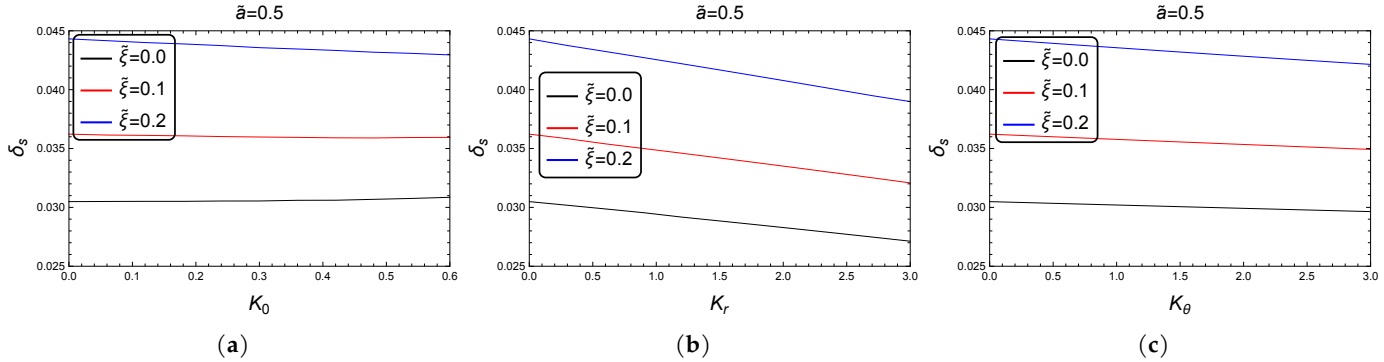


Figure 6. Variation in the distortion parameter δ_s of the rotating ASG black hole with the plasma parameter for different plasma models. The spin parameter is $\tilde{a} = 0.5$, and the black, red, and blue curves correspond to $\tilde{\xi} = 0,\ 0.1,\ 0.2$, respectively. (**a**) Homogeneous plasma. (**b**) Radially inhomogeneous plasma. (**c**) Angularly inhomogeneous plasma.

Overall, as the ASG correction parameter $\tilde{\xi}$ increases, the overall size of the shadow decreases, while its deviation from circularity increases. Homogeneous plasma enlarges the shadow, while its effect on the shadow shape depends on the ASG quantum correction. Radially and angularly inhomogeneous plasmas, in contrast, reduce the shadow size and make the shadow more circular. Between the two inhomogeneous plasma distributions, angularly inhomogeneous plasma has a more pronounced effect on the shadow size, whereas radially inhomogeneous plasma has a more significant effect on the shadow shape.

4.2. Parameter Estimation Using Shadow Area and Oblateness

Kumar and Ghosh proposed a method for estimating BH parameters by combining the shadow area A and oblateness D, and applied it to the parameter estimation of Kerr, Kerr–Newman, and rotating regular BHs [101]. This method was subsequently employed to estimate the parameters of other rotating BH models [102,103]. The method involves

plotting the contours of the shadow area A and oblateness D in a two-dimensional parameter space. When the two contours intersect at a unique point, the corresponding two parameters can be determined from the intersection [101].

Based on the above method, we take the radially inhomogeneous plasma as an example and fix the spin parameter at $\tilde{a} = 0.5$. We plot the contours of the shadow area A/M^2 and oblateness D in the $(\tilde{\xi}, K_r)$ parameter plane, as shown in Figure 7. Given the ranges of A/M^2 and D shown above, several values are selected to plot the corresponding contours. It can be seen that, for a given value of either A/M^2 or D, the corresponding contour represents a series of $(\tilde{\xi}, K_r)$ parameter combinations, and thus a single observable cannot simultaneously determine the two model parameters. Furthermore, the contours of A/M^2 and D exhibit different trends and intersect in the parameter plane. For a given pair of A/M^2 and D, the corresponding $(\tilde{\xi}, K_r)$ can be inferred from the intersection of the two contours within the parameter range considered. Table 1 lists several combinations of A/M^2 and D together with their corresponding parameter values. Since observational uncertainties and correlations between the observables have not been taken into account in this work, the results presented in Figure 7 and Table 1 are mainly intended to illustrate the parameter estimation method within the theoretical model.

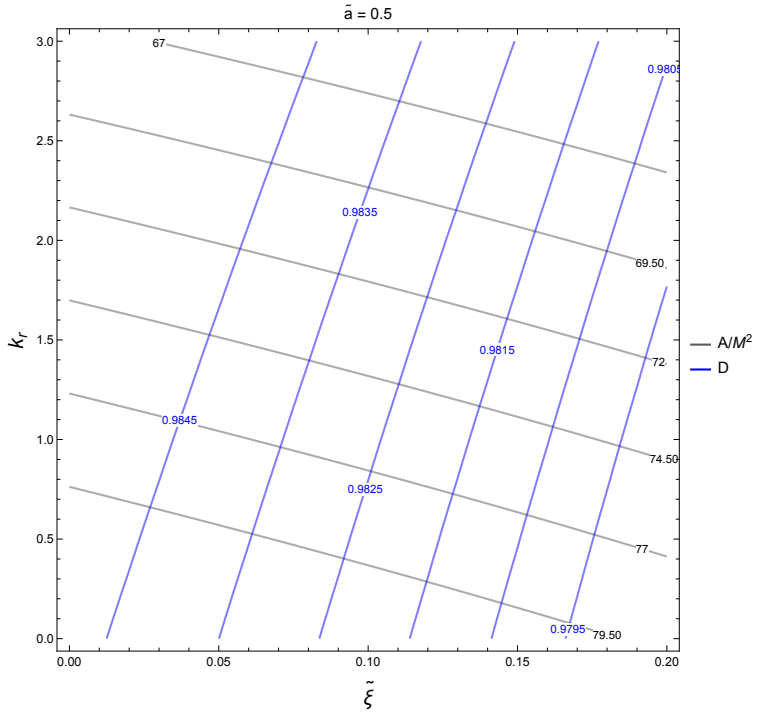


Figure 7. Contours of the shadow area A/M^2 and oblateness D in the $(\tilde{\xi}, K_r)$ parameter plane for a radially inhomogeneous plasma. The spin parameter is fixed at $\tilde{a} = 0.5$.

Table 1. Parameter estimates of $(\tilde{\xi}, K_r)$ obtained from the intersections of contours for given A/M^2 and D in a radially inhomogeneous plasma. The spin parameter is fixed at $\tilde{a} = 0.5$.

A/M^2	D	$\tilde{\xi}$	K_r
67.0	0.9845	0.0782	2.8191
67.0	0.9835	0.1105	2.6987
67.0	0.9825	0.1394	2.5870
72.0	0.9825	0.1198	1.7149
74.5	0.9825	0.1103	1.2779
77.0	0.9825	0.1010	0.8403

5. Constraints on Model Parameters from Sgr A* Shadow Observations

Horizon-scale images of supermassive BHs obtained by the EHT provide an important observational basis for probing the properties of spacetime in the strong field regime through BH shadows [65,67,79]. In recent years, comparisons between theoretically calculated shadow observables and EHT observations have been used to constrain the parameters of various BH spacetimes [104–109]. In this work, we use EHT observations of the Sgr A* shadow to constrain the ASG correction parameter $\tilde{\xi}$ and the radially inhomogeneous plasma parameter K_r.

We next consider the shadow angular diameter $\theta_{\rm sh}$ and its deviation parameter δ relative to the Schwarzschild shadow diameter. The shadow diameter $d_{\rm sh}$ is related to the shadow area A by [102,103]:

$$d_{\rm sh} = 2\sqrt{A/\pi}. \tag{42}$$

When the distance between the BH and the observer is d, the corresponding angular shadow diameter is given by

$$\theta_{\rm sh} = \frac{2}{d}\sqrt{\frac{A}{\pi}}. \tag{43}$$

On the other hand, taking the Schwarzschild shadow diameter $6\sqrt{3}M$ as the reference value, the deviation parameter δ is defined as [65,67]

$$\delta = \frac{d_{\rm sh}}{6\sqrt{3}M} - 1. \tag{44}$$

To compare the shadow of the rotating ASG BH obtained in this work with the observational results for Sgr A*, we adopt its mass $M = 4.0\times10^6 M_\odot$ and the distance between the BH and Earth, $d = 8.15\,\mathrm{kpc}$ [65,79]. For simplicity, we do not consider the uncertainties in the mass and distance measurements of Sgr A* in the present analysis. The EHT Collaboration measured a bright emission-ring diameter of 51.8 ± 2.3 μas for Sgr A* [79]. Using simulated images, the EHT Collaboration calibrated the relationship between the measured emission-ring diameter and the geometrically defined black hole shadow diameter, and inferred the shadow angular diameter under the adopted model assumptions to be [65]:

$$\theta_{\rm sh} = 48.7 \pm 7.0\ \mu\mathrm{as}. \tag{45}$$

In addition, based on measurements of the mass and distance of Sgr A* by Keck and the Very Large Telescope Interferometer (VLTI), the EHT Collaboration reported the corresponding deviation parameters as [65]

$$\delta_{\rm Keck} = -0.04^{+0.09}_{-0.10}, \qquad \delta_{\rm VLTI} = -0.08^{+0.09}_{-0.09}. \tag{46}$$

Within the adopted cold, nonmagnetized, radially inhomogeneous plasma model, we obtain approximate constraints on the $(\tilde{\xi}, K_r)$ parameter space by comparing our theoretical shadow observables with the shadow angular diameter and deviation parameters reported by the EHT Collaboration for Sgr A*. The spin parameter affects the critical impact parameters λ and η of unstable spherical photon orbits, thereby influencing the celestial coordinates of the shadow boundary. The observer inclination also affects the projection of critical photon trajectories onto the observer's sky. These effects may change the predicted shadow angular diameter and deviation parameter, and hence the region of the $(\tilde{\xi}, K_r)$ parameter space consistent with the EHT observations. For the observational constraints considered here, we choose an equatorial observer with $\theta_o = \pi/2$ and fix the spin parameter at $\tilde{a} = 0.5$. In addition, the parameter values are required to satisfy the condition for the existence of an event horizon obtained in Section 2. According to Equations (43) and (44), we calculate the angular shadow diameter $\theta_{\rm sh}$ and deviation parameter δ as functions of $(\tilde{\xi}, K_r)$,

as shown in Figures 8 and 9, respectively. The red dashed curve represents the boundary determined by the condition for the existence of an event horizon, separating the BH region on the left from the region without an event horizon. It can be seen that both $\theta_{\rm sh}$ and δ gradually decrease as either $\tilde{\xi}$ or K_r increases. The black solid curve in Figure 8 corresponds to $\theta_{\rm sh} = 41.7\,\mu$as, and the region below this curve satisfies the EHT observational constraint on the angular shadow diameter of Sgr A*. Within the parameter range considered in this work, the theoretically calculated values of δ do not exceed the corresponding observational upper limits, and therefore the constraint on the parameter space is determined solely by the observational lower limits. The black solid curves in Figure 9a,b correspond to $\delta = -0.14$ and $\delta = -0.17$, respectively, and the regions below these curves satisfy the observational constraints from Keck and VLTI, respectively. Compared with the Keck constraint, the VLTI constraint corresponds to a larger allowed parameter region. For example, when $\tilde{\xi} = 0.1$ is fixed, the upper limits on K_r obtained from the observational constraints on the angular shadow diameter and the deviation parameters from Keck and VLTI are 4.391, 3.539, and 4.345, respectively, with the Keck observation providing the tightest constraint. Under the above conditions, within the adopted cold, nonmagnetized, radially inhomogeneous plasma model and the parameter range considered in this work, the constraints derived from the EHT observations of Sgr A* at approximately 230 GHz [79] mainly disfavor the region of parameter space in which both $\tilde{\xi}$ and K_r take relatively large values.

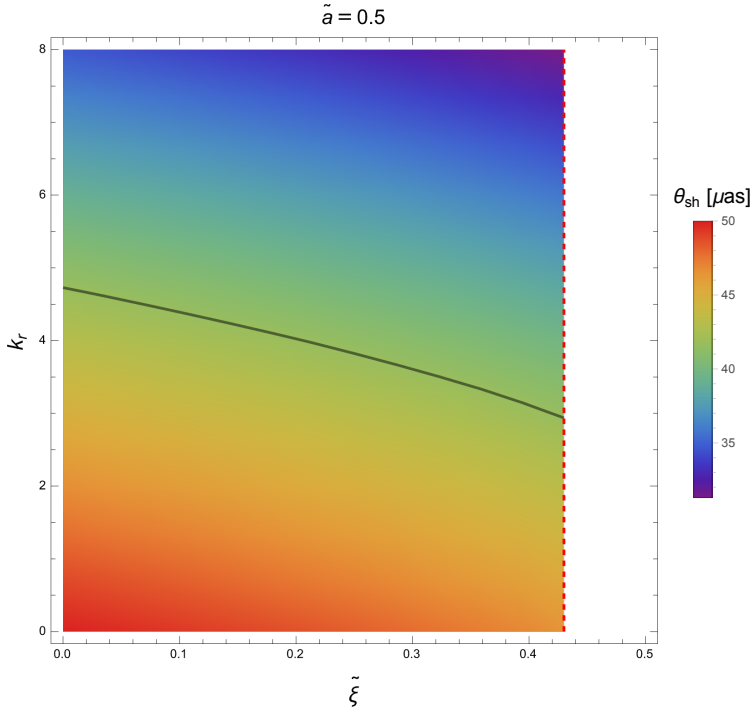


Figure 8. Constraint on the $(\tilde{\xi}, K_r)$ parameter space from observations of the Sgr A* shadow angular diameter $\theta_{\rm sh}$. The spin parameter is fixed at $\tilde{a} = 0.5$, and the observer is located in the equatorial plane, $\theta_o = \pi/2$. The red dashed curve represents the boundary of the parameter space determined by the condition for the existence of an event horizon, while the black solid curve corresponds to $\theta_{\rm sh} = 41.7\,\mu$as.

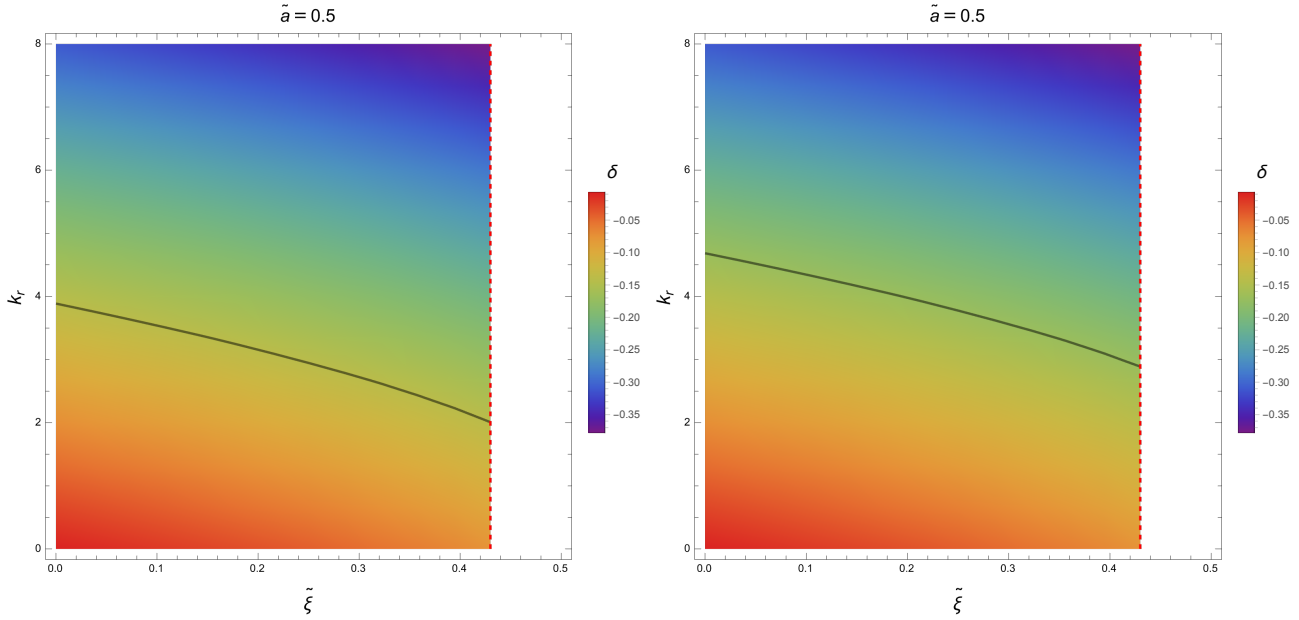


Figure 9. Constraint on the $(\tilde{\xi}, K_r)$ parameter space from observations of the Sgr A* shadow deviation parameter δ. The spin parameter is fixed at $\tilde{a} = 0.5$, and the observer is located in the equatorial plane, $\theta_o = \pi/2$. The red dashed curve represents the boundary of the parameter space determined by the condition for the existence of an event horizon, while the black solid curves correspond to (**a**) $\delta = -0.14$ for Keck and (**b**) $\delta = -0.17$ for VLTI.

6. Conclusions

This work investigated photon motion and shadow properties of rotating BHs in asymptotically safe gravity in the presence of plasma. In the infrared limit of ASG, we incorporated the ASG correction described by a running Newton coupling and analyzed the event horizon and parameter space of rotating ASG BHs. The results show that the allowed range of the ASG correction parameter $\tilde{\xi}$ is restricted by the spin parameter $\tilde{a}$. As $\tilde{a}$ increases, the range of $\tilde{\xi}$ permitted by the condition for the existence of an event horizon gradually decreases.

We further investigated the effects of the plasma environment surrounding the BH on photon motion and shadow properties. For plasma distributions satisfying the separability condition of the Hamilton–Jacobi equation, we considered three distributions, namely homogeneous, radially inhomogeneous, and angularly inhomogeneous plasmas, and determined the corresponding shadow boundaries from unstable spherical photon orbits. Within the parameter range considered in this work, for a fixed spin parameter $\tilde{a} = 0.5$ and an equatorial observer, the shadow size increases with increasing K_0 in a homogeneous plasma, while it decreases with increasing K_r and K_θ in radially and angularly inhomogeneous plasmas, respectively. For fixed plasma parameters, the shadow size decreases with increasing $\tilde{\xi}$ for all three plasma models. Regarding the shadow shape, the deviation from circularity generally increases with increasing $\tilde{\xi}$. Radially and angularly inhomogeneous plasmas make the shadow progressively more circular, while the effect of homogeneous plasma on the shadow shape depends on the ASG correction parameter $\tilde{\xi}$. Overall, within the parameter ranges considered, plasma changes are more pronounced in the shadow size observables than in the shape observables. Comparing the two inhomogeneous plasma models, angularly inhomogeneous plasma has a stronger effect on the shadow size, whereas radially inhomogeneous plasma has a more pronounced effect on the shadow shape. In addition, taking radially inhomogeneous plasma as an example and fixing $\tilde{a} = 0.5$, we estimated

the model parameters using the contours of the shadow area A/M^2 and oblateness D in the $(\tilde{\xi}, K_r)$ parameter plane. For a given pair of A/M^2 and D, the values of $\tilde{\xi}$ and K_r can be determined from the unique intersection of the corresponding contours.

Finally, we used the EHT observational results for the Sgr A* shadow, including the shadow angular diameter $\theta_{\rm sh}$ and the deviation parameters δ obtained using the Keck and VLTI measurements, to constrain the $(\tilde{\xi}, K_r)$ parameter space in a radially inhomogeneous plasma. Imposing the condition for the existence of an event horizon and fixing $\tilde{a} = 0.5$ and $\theta_o = \pi/2$, both $\theta_{\rm sh}$ and δ decrease as either $\tilde{\xi}$ or K_r increases. The results show that the shadow observations of Sgr A* mainly disfavor the region of parameter space where both $\tilde{\xi}$ and K_r take relatively large values. Within the adopted infrared approximation, these results provide a theoretical reference for understanding the effects of the ASG correction and the plasma environment on black hole shadows, as well as for exploring their observational implications.

Author Contributions: Conceptualization, M.X. and J.L.; methodology, M.X.; software, M.X.; validation, M.X., H.C., L.G. and Z.G.; formal analysis, M.X.; investigation, M.X.; writing—original draft preparation, M.X.; writing—review and editing, H.C., L.G., Z.G. and J.L.; visualization, M.X.; supervision, J.L.; project administration, J.L.; funding acquisition, J.L. All authors have read and agreed to the published version of the manuscript.

Funding: This research was funded by the National Natural Science Foundation of China, grant numbers 12675070 and 12175095, and the Liaoning Revitalization Talents Program, grant number XLYC2007047.

Data Availability Statement: No new data were created or analyzed in this study. Data sharing is not applicable to this article.

Conflicts of Interest: The authors declare no conflicts of interest.

References

1. Will, C.M. The confrontation between general relativity and experiment. *Living Rev. Relativ.* **2014**, *17*, 4. [CrossRef] [PubMed]
2. Yunes, N.; Siemens, X.; Yagi, K. Gravitational-wave tests of general relativity with ground-based detectors and pulsar-timing arrays. *Living Rev. Relativ.* **2025**, *28*, 3. [CrossRef]
3. Lu, J.; Liu, M.; Wu, Y.; Wang, Y.; Yang, W. Cosmic constraint on massive neutrinos in viable $f(R)$ gravity with producing ΛCDM background expansion. *Eur. Phys. J. C* **2016**, *76*, 679. [CrossRef]
4. Lu, J.; Chee, G. Cosmology in Poincaré gauge gravity with a pseudoscalar torsion. *J. High Energy Phys.* **2016**, *5*, 24. [CrossRef]
5. Lu, J.; Geng, D.; Xu, L.; Wu, Y.; Liu, M. Reduced modified Chaplygin gas cosmology. *J. High Energy Phys.* **2015**, *2*, 71. [CrossRef]
6. Lu, J.; Xu, L.; Liu, M.; Gui, Y. Constraints on accelerating universe using ESSENCE and Gold supernovae data combined with other cosmological probes. *Eur. Phys. J. C* **2008**, *58*, 311–324. [CrossRef]
7. Goroff, M.H.; Sagnotti, A. The ultraviolet behavior of Einstein gravity. *Nucl. Phys. B* **1986**, *266*, 709–736. [CrossRef]
8. Eichhorn, A. An asymptotically safe guide to quantum gravity and matter. *Front. Astron. Space Sci.* **2019**, *5*, 47. [CrossRef]
9. Donoghue, J.F. General relativity as an effective field theory: The leading quantum corrections. *Phys. Rev. D* **1994**, *50*, 3874–3888. [CrossRef] [PubMed]
10. Weinberg, S. Ultraviolet divergences in quantum theories of gravitation. In *General Relativity: An Einstein Centenary Survey*; Hawking, S.W., Israel, W., Eds.; Cambridge University Press: Cambridge, UK, 1979; pp. 790–831.
11. Bonanno, A.; Eichhorn, A.; Gies, H.; Pawlowski, J.M.; Percacci, R.; Reuter, M.; Saueressig, F.; Vacca, G.P. Critical reflections on asymptotically safe gravity. *Front. Phys.* **2020**, *8*, 269. [CrossRef]
12. Reuter, M. Nonperturbative evolution equation for quantum gravity. *Phys. Rev. D* **1998**, *57*, 971–985. [CrossRef]
13. Niedermaier, M.; Reuter, M. The asymptotic safety scenario in quantum gravity. *Living Rev. Relativ.* **2006**, *9*, 5. [CrossRef] [PubMed]
14. Becker, M.; Kurov, A.; Saueressig, F. Remarks on the origin of almost-Gaussian scaling in asymptotically safe quantum gravity. *Phys. Rev. D* **2024**, *110*, 126003. [CrossRef]
15. Bonanno, A.; Malafarina, D.; Panassiti, A. Dust collapse in asymptotic safety: A path to regular black holes. *Phys. Rev. Lett.* **2024**, *132*, 031401. [CrossRef] [PubMed]

16. Pawlowski, J.M.; Tränkle, J. Effective action and black hole solutions in asymptotically safe quantum gravity. *Phys. Rev. D* **2024**, *110*, 086011. [CrossRef]
17. Chen, C.-M.; Mandal, R.; Ohta, N. On the cutoff scale identification of FLRW cosmology in asymptotically safe gravity. *Class. Quantum Grav.* **2025**, *42*, 095011. [CrossRef]
18. Silva, A. Emergence of inflaton potential from asymptotically safe gravity. *Phys. Lett. B* **2025**, *860*, 139154. [CrossRef]
19. Harada, T.; Chen, C.-M.; Mandal, R. Singularity resolution and regular black hole formation in gravitational collapse in asymptotically safe gravity. *Phys. Rev. D* **2025**, *111*, 126017. [CrossRef]
20. Chen, C.-M.; Ishibashi, A.; Mandal, R.; Ohta, N. Bianchi-I cosmology with scale dependent G and Λ in asymptotically safe gravity. *Class. Quantum Grav.* **2025**, *42*, 235008. [CrossRef]
21. Mustafa, G.; Alimova, A.; Atamurotov, F.; Ibraheem, A.A.; Channuie, P.; Bahaddinova, G. Testing regular black holes in the framework of asymptotically safe gravity using particle dynamics, QPOs, and shadow constraints. *Eur. Phys. J. C* **2025**, *85*, 741. [CrossRef]
22. Falls, K.; Litim, D.F.; Raghuraman, A. Black holes and asymptotically safe gravity. *Int. J. Mod. Phys. A* **2012**, *27*, 1250019. [CrossRef]
23. Koch, B.; Saueressig, F. Black holes within asymptotic safety. *Int. J. Mod. Phys. A* **2014**, *29*, 1430011. [CrossRef]
24. Eichhorn, A.; Held, A. Black holes in asymptotically safe gravity and beyond. In *Regular Black Holes: Towards a New Paradigm of Gravitational Collapse*; Bambi, C., Ed.; Springer: Singapore, 2023; pp. 131–183. [CrossRef]
25. Bonanno, A.; Reuter, M. Renormalization group improved black hole spacetimes. *Phys. Rev. D* **2000**, *62*, 043008. [CrossRef]
26. Bonanno, A.; Reuter, M. Spacetime structure of an evaporating black hole in quantum gravity. *Phys. Rev. D* **2006**, *73*, 083005. [CrossRef]
27. Cai, Y.-F.; Easson, D.A. Black holes in an asymptotically safe gravity theory with higher derivatives. *J. Cosmol. Astropart. Phys.* **2010**, *9*, 002. [CrossRef]
28. Reuter, M.; Tuiran, E. Quantum gravity effects in the Kerr spacetime. *Phys. Rev. D* **2011**, *83*, 044041. [CrossRef]
29. Lambiase, G.; Pantig, R.C.; Gogoi, D.J.; Övgün, A. Investigating the connection between generalized uncertainty principle and asymptotically safe gravity in black hole signatures through shadow and quasinormal modes. *Eur. Phys. J. C* **2023**, *83*, 679. [CrossRef]
30. Stashko, O. Quasinormal modes and gray-body factors of regular black holes in asymptotically safe gravity. *Phys. Rev. D* **2024**, *110*, 084016. [CrossRef]
31. Dubinsky, A. Quasinormal modes of charged black holes in Asymptotically Safe Gravity. *Phys. Dark Universe* **2024**, *46*, 101657. [CrossRef]
32. Kumar, R.; Singh, B.P.; Ghosh, S.G. Shadow and deflection angle of rotating black hole in asymptotically safe gravity. *Ann. Phys.* **2020**, *420*, 168252. [CrossRef]
33. Sánchez, L.A. Shadow of a renormalization group improved rotating black hole. *Eur. Phys. J. C* **2024**, *84*, 1056. [CrossRef]
34. Urmanov, A.; Chakrabarty, H.; Malafarina, D. Observational properties of regular black holes in asymptotic safety. *Eur. Phys. J. C* **2025**, *85*, 642. [CrossRef]
35. Bhattacharjee, C.; Sau, S.; Mukherjee, A. Radiative and jet signatures of regular black holes in quantum-corrected gravity: Constraints from disk efficiency and jet power in asymptotically safe spacetime. *Eur. Phys. J. C* **2025**, *85*, 1071. [CrossRef]
36. Lütfüoğlu, B.C. Quasinormal modes and gray-body factors for gravitational perturbations in asymptotically safe gravity. *Eur. Phys. J. C* **2026**, *86*, 39. [CrossRef]
37. Haroon, S.; Jamil, M.; Lin, K.; Pavlovic, P.; Sossich, M.; Wang, A. The effects of running gravitational coupling on rotating black holes. *Eur. Phys. J. C* **2018**, *78*, 519. [CrossRef]
38. Donmez, O.; Ghosh, S.G.; Yousaf, M.; Mustafa, G.; Atamurotov, F. Accretion flow around Kerr metric in the infra-red limit of asymptotically safe gravity. *J. Cosmol. Astropart. Phys.* **2026**, *04*, 045. [CrossRef]
39. Lu, J.; Wu, X. Chaos of charged particles near a renormalized group improved Kerr black hole in an external magnetic field. *Eur. Phys. J. C* **2025**, *85*, 1122. [CrossRef]
40. Kala, S.; Singh, P.; Nandan, H.; Yousaf, M.; Atamurotov, F.; Mustafa, G. Infrared signatures of asymptotically safe gravity on chaos with weighted Birkhoff average in the Kerr black hole. *Phys. Lett. B* **2026**, *879*, 140597. [CrossRef]
41. Zhang, Y.; Zhou, M.; Bambi, C. Iron line spectroscopy of black holes in asymptotically safe gravity. *Eur. Phys. J. C* **2018**, *78*, 376. [CrossRef]
42. Sánchez, L.A. Quantum gravity modifications to the accretion onto a Kerr black hole. *Eur. Phys. J. C* **2024**, *84*, 635. [CrossRef]
43. Abbott, B.P.; Abbott, R.; Abbott, T.D.; Abernathy, M.R.; Acernese, F.; Ackley, K.; Adams, C.; Adams, T.; Addesso, P.; Adhikari, R.X.; et al. Observation of gravitational waves from a binary black hole merger. *Phys. Rev. Lett.* **2016**, *116*, 061102. [CrossRef] [PubMed]
44. Zhao, Y.; Dai, N.; Gong, Y. Distinguishing dark matter haloes with extreme mass ratio inspirals. *Mon. Not. R. Astron. Soc.* **2025**, *543*, 2326–2337. [CrossRef]

45. Shen, Z.; Wang, A.; Gong, Y.; Yin, S. Analytical models of supermassive black holes in galaxies surrounded by dark matter halos. *Phys. Lett. B* **2024**, *855*, 138797. [CrossRef]
46. Zhang, C.; Guo, H.; Gong, Y.; Wang, B. Detecting vector charge with extreme mass ratio inspirals onto Kerr black holes. *J. Cosmol. Astropart. Phys.* **2023**, *6*, 020. [CrossRef]
47. Yang, S.; Lu, J.; Li, W.; Xu, M.; Xu, J. Observational constraints on the Kerr and its several single-parameter modified spacetimes using quasi-periodic oscillation data. *Eur. Phys. J. C* **2025**, *85*, 894. [CrossRef]
48. Lu, J.; Xu, M.; Guo, J.; Li, R. Investigating the physical properties of traversable wormholes in the modified $f(R,T)$ gravity. *Gen. Relativ. Gravit.* **2024**, *56*, 37. [CrossRef]
49. Virbhadra, K.S.; Ellis, G.F.R. Schwarzschild black hole lensing. *Phys. Rev. D* **2000**, *62*, 084003. [CrossRef]
50. Bozza, V. Gravitational lensing in the strong field limit. *Phys. Rev. D* **2002**, *66*, 103001. [CrossRef]
51. Tsukamoto, N. Deflection angle in the strong deflection limit in a general asymptotically flat, static, spherically symmetric spacetime. *Phys. Rev. D* **2017**, *95*, 064035. [CrossRef]
52. Falcke, H.; Melia, F.; Agol, E. Viewing the shadow of the black hole at the Galactic center. *Astrophys. J. Lett.* **2000**, *528*, L13–L16. [CrossRef] [PubMed]
53. Cunha, P.V.P.; Herdeiro, C.A.R. Shadows and strong gravitational lensing: A brief review. *Gen. Relativ. Gravit.* **2018**, *50*, 42. [CrossRef]
54. Gralla, S.E.; Holz, D.E.; Wald, R.M. Black hole shadows, photon rings, and lensing rings. *Phys. Rev. D* **2019**, *100*, 024018. [CrossRef]
55. Grenzebach, A.; Perlick, V.; Lämmerzahl, C. Photon regions and shadows of Kerr-Newman-NUT black holes with a cosmological constant. *Phys. Rev. D* **2014**, *89*, 124004. [CrossRef]
56. Perlick, V.; Tsupko, O.Y. Calculating black hole shadows: Review of analytical studies. *Phys. Rep.* **2022**, *947*, 1–39. [CrossRef]
57. Liu, W.; Wu, D.; Wang, J. Light rings and shadows of static black holes in effective quantum gravity II: A new solution without Cauchy horizons. *Phys. Lett. B* **2025**, *868*, 139742. [CrossRef]
58. Guo, M.; Li, P.-C. Innermost stable circular orbit and shadow of the 4D Einstein–Gauss–Bonnet black hole. *Eur. Phys. J. C* **2020**, *80*, 588. [CrossRef]
59. Li, L.-Y.; Liu, X.-Y.; Cai, R.-G.; Gong, Y.; Zhou, W. Images and photon regions of continuous photon sphere spacetime. *Phys. Dark Universe* **2026**, *51*, 102209. [CrossRef]
60. Xu, M.; Lu, J.; Liu, Y.; Gao, Y.; Wu, S. Photon motion and shadows of rotating black holes with nonlinear electromagnetic and anisotropic matter fields. *Eur. Phys. J. Plus* **2026**, *141*, 1212. [CrossRef]
61. Psaltis, D. Testing general relativity with the Event Horizon Telescope. *Gen. Relativ. Gravit.* **2019**, *51*, 137. [CrossRef]
62. Liu, W.; Huang, H.; Wu, D.; Wang, J. Lorentz violation signatures in the low-energy sector of Hořava gravity from black hole shadow observations. *Phys. Lett. B* **2025**, *868*, 139812. [CrossRef]
63. Psaltis, D.; Medeiros, L.; Christian, P.; Özel, F.; Akiyama, K.; Alberdi, A.; Alef, W.; Asada, K.; Azulay, R.; Ball, D.; et al. Gravitational test beyond the first post-Newtonian order with the shadow of the M87 black hole. *Phys. Rev. Lett.* **2020**, *125*, 141104. [CrossRef] [PubMed]
64. Hou, Y.; Guo, M.; Chen, B. Revisiting the shadow of braneworld black holes. *Phys. Rev. D* **2021**, *104*, 024001. [CrossRef]
65. Event Horizon Telescope Collaboration. First Sagittarius A* Event Horizon Telescope results. VI. Testing the black hole metric. *Astrophys. J. Lett.* **2022**, *930*, L17. [CrossRef]
66. Liu, W.; Liu, Y.; Wu, D.; Liu, Y.-X. Universal framework for horizon-scale tests of gravity with black hole shadows. *Phys. Rev. D* **2026**, *114*, L021503. [CrossRef]
67. Vagnozzi, S.; Roy, R.; Tsai, Y.-D.; Visinelli, L.; Afrin, M.; Allahyari, A.; Bambhaniya, P.; Dey, D.; Ghosh, S.G.; Joshi, P.S.; et al. Horizon-scale tests of gravity theories and fundamental physics from the Event Horizon Telescope image of Sagittarius A*. *Class. Quantum Grav.* **2023**, *40*, 165007. [CrossRef]
68. Wei, S.-W.; Wang, C.-H.; Zhang, Y.-P.; Liu, Y.-X.; Mann, R.B. Gravitational equal-area law and critical phenomena of cuspy black hole shadow. *Phys. Rev. D* **2026**, *114*, 044082. [CrossRef]
69. Wang, X.; Zhao, Z.; Zeng, X.-X.; Wang, X.-Y. Revisiting the shadow of Johannsen-Psaltis black holes. *Phys. Rev. D* **2025**, *111*, 084054. [CrossRef]
70. Uniyal, A.; Dihingia, I.K.; Mizuno, Y.; Rezzolla, L. The future ability to test theories of gravity with black-hole shadows. *Nat. Astron.* **2026**, *10*, 165–172. [CrossRef]
71. Liu, W.; Wu, D.; Fang, X.; Jing, J.; Wang, J. Kerr-MOG-(A)dS black hole and its shadow in scalar-tensor-vector gravity theory. *J. Cosmol. Astropart. Phys.* **2024**, *8*, 035. [CrossRef]
72. Zhang, Z.; Hou, Y.; Guo, M. Observational signatures of rotating black holes in the semiclassical gravity with trace anomaly. *Chin. Phys. C* **2024**, *48*, 085106. [CrossRef]
73. Li, L.-Y.; Cao, L.-M.; Gong, Y.; Liu, X.-Y.; Zhou, W. Signatures of the Israel junction II: Double photon rings in slowly rotating Kerr spacetime with thin shell. *Eur. Phys. J. C* **2026**, *86*, 704. [CrossRef]

74. Doeleman, S.S.; Weintroub, J.; Rogers, A.E.E.; Plambeck, R.; Freund, R.; Tilanus, R.P.J.; Friberg, P.; Ziurys, L.M.; Moran, J.M.; Corey, B.; et al. Event-horizon-scale structure in the supermassive black hole candidate at the Galactic Centre. *Nature* **2008**, *455*, 78–80. [CrossRef] [PubMed]
75. Event Horizon Telescope Collaboration. First M87 Event Horizon Telescope results. II. Array and instrumentation. *Astrophys. J. Lett.* **2019**, *875*, L2. [CrossRef]
76. Event Horizon Telescope Collaboration. First M87 Event Horizon Telescope results. I. The shadow of the supermassive black hole. *Astrophys. J. Lett.* **2019**, *875*, L1. [CrossRef]
77. Event Horizon Telescope Collaboration. First M87 Event Horizon Telescope results. IV. Imaging the central supermassive black hole. *Astrophys. J. Lett.* **2019**, *875*, L4. [CrossRef]
78. Event Horizon Telescope Collaboration. First M87 Event Horizon Telescope results. VI. The shadow and mass of the central black hole. *Astrophys. J. Lett.* **2019**, *875*, L6. [CrossRef]
79. Event Horizon Telescope Collaboration. First Sagittarius A* Event Horizon Telescope results. I. The shadow of the supermassive black hole in the center of the Milky Way. *Astrophys. J. Lett.* **2022**, *930*, L12. [CrossRef]
80. Event Horizon Telescope Collaboration. First Sagittarius A* Event Horizon Telescope results. III. Imaging of the Galactic Center supermassive black hole. *Astrophys. J. Lett.* **2022**, *930*, L14. [CrossRef]
81. Event Horizon Telescope Collaboration. First M87 Event Horizon Telescope results. V. Physical origin of the asymmetric ring. *Astrophys. J. Lett.* **2019**, *875*, L5. [CrossRef]
82. Event Horizon Telescope Collaboration. First Sagittarius A* Event Horizon Telescope results. V. Testing astrophysical models of the Galactic Center black hole. *Astrophys. J. Lett.* **2022**, *930*, L16. [CrossRef]
83. Yang, S.; Lu, J.; Xu, M.; Liu, Y. Constraining magnetized black-bounce spacetime from HFQPOs data and selecting resonance models via information criteria and Bayesian analysis. *Eur. Phys. J. C* **2026**, *86*, 1233. [CrossRef]
84. Perlick, V.; Tsupko, O.Y.; Bisnovatyi-Kogan, G.S. Influence of a plasma on the shadow of a spherically symmetric black hole. *Phys. Rev. D* **2015**, *92*, 104031. [CrossRef]
85. Perlick, V.; Tsupko, O.Y. Light propagation in a plasma on Kerr spacetime: Separation of the Hamilton-Jacobi equation and calculation of the shadow. *Phys. Rev. D* **2017**, *95*, 104003. [CrossRef]
86. Badía, J.; Eiroa, E.F. Shadow of axisymmetric, stationary, and asymptotically flat black holes in the presence of plasma. *Phys. Rev. D* **2021**, *104*, 084055. [CrossRef]
87. Zhang, Z.; Yan, H.; Guo, M.; Chen, B. Shadows of Kerr black holes with a Gaussian-distributed plasma in the polar direction. *Phys. Rev. D* **2023**, *107*, 024027. [CrossRef]
88. Briozzo, G.; Gallo, E.; Mädler, T. Shadows of rotating black holes in plasma environments with aberration effects. *Phys. Rev. D* **2023**, *107*, 124004. [CrossRef]
89. Badía, J.; Eiroa, E.F. Shadows of rotating Einstein–Maxwell–dilaton black holes surrounded by a plasma. *Phys. Rev. D* **2023**, *107*, 124028. [CrossRef]
90. Wang, H.-M.; Wei, S.-W. Shadow cast by Kerr-like black hole in the presence of plasma in Einstein-bumblebee gravity. *Eur. Phys. J. Plus* **2022**, *137*, 571. [CrossRef]
91. Zuluaga, F.H.; Sánchez, L.A. Accretion disk around a Schwarzschild black hole in asymptotic safety. *Eur. Phys. J. C* **2021**, *81*, 840. [CrossRef]
92. Azreg-Aïnou, M. Generating rotating regular black hole solutions without complexification. *Phys. Rev. D* **2014**, *90*, 064041. [CrossRef]
93. Turakhonov, Z.; Atamurotov, F.; Ghosh, S.G.; Abdujabbarov, A. Probing effects of plasma on shadow and weak gravitational lensing by regular black holes in asymptotically safe gravity. *Phys. Dark Universe* **2025**, *48*, 101880. [CrossRef]
94. Xu, M.; Li, R.; Lu, J.; Yang, S.; Wu, S. Optical appearance and shadow of Kalb–Ramond black hole: Effects of plasma and accretion models. *Eur. Phys. J. C* **2025**, *85*, 676. [CrossRef]
95. Carter, B. Global structure of the Kerr family of gravitational fields. *Phys. Rev.* **1968**, *174*, 1559–1571. [CrossRef]
96. Liu, W.; Wu, D.; Wang, J. Light rings and shadows of static black holes in effective quantum gravity. *Phys. Lett. B* **2024**, *858*, 139052. [CrossRef]
97. Peng, J.; Guo, M.; Feng, X.-H. Influence of quantum correction on black hole shadows, photon rings, and lensing rings. *Chin. Phys. C* **2021**, *45*, 085103. [CrossRef]
98. Bardeen, J.M. Timelike and null geodesics in the Kerr metric. In *Black Holes (Les Astres Occlus)*; DeWitt, C., DeWitt, B.S., Eds.; Gordon and Breach: New York, NY, USA, 1973; pp. 215–240.
99. Shapiro, S.L. Accretion onto black holes: The emergent radiation spectrum. III. Rotating (Kerr) black holes. *Astrophys. J.* **1974**, *189*, 343–352. [CrossRef]
100. Hioki, K.; Maeda, K. Measurement of the Kerr spin parameter by observation of a compact object's shadow. *Phys. Rev. D* **2009**, *80*, 024042. [CrossRef]
101. Kumar, R.; Ghosh, S.G. Black hole parameter estimation from its shadow. *Astrophys. J.* **2020**, *892*, 78. [CrossRef]

102. Afrin, M.; Kumar, R.; Ghosh, S.G. Parameter estimation of hairy Kerr black holes from its shadow and constraints from M87*. *Mon. Not. R. Astron. Soc.* **2021**, *504*, 5927–5940. [CrossRef]
103. Afrin, M.; Vagnozzi, S.; Ghosh, S.G. Tests of loop quantum gravity from the Event Horizon Telescope results of Sgr A*. *Astrophys. J.* **2023**, *944*, 149. [CrossRef]
104. Kuang, X.-M.; Tang, Z.-Y.; Wang, B.; Wang, A. Constraining a modified gravity theory in strong gravitational lensing and black hole shadow observations. *Phys. Rev. D* **2022**, *106*, 064012. [CrossRef]
105. Wu, Y.; Cai, Z.; Ban, Z.; Feng, H.; Chen, W.-Q. Probing Einstein–Maxwell-scalar black hole via thin accretion disks and shadows with EHT observations of M87* and Sgr A*. *Eur. Phys. J. C* **2025**, *85*, 1085. [CrossRef]
106. Yasmin, S.; Jafarzade, K.; Jamil, M. Shadow cast by the Kerr MOG black hole under the influence of plasma and constraints from EHT observations. *Chin. Phys. C* **2025**, *49*, 065107. [CrossRef]
107. Liu, W.; Wu, D.; Wang, J. Shadow of slowly rotating Kalb–Ramond black holes. *J. Cosmol. Astropart. Phys.* **2025**, *5*, 017. [CrossRef]
108. Liu, J.-Z.; Guo, W.-D.; Wei, S.-W.; Liu, Y.-X. Charged spherically symmetric and slowly rotating charged black hole solutions in bumblebee gravity. *Eur. Phys. J. C* **2025**, *85*, 145. [CrossRef]
109. Xu, M.; Lu, J.; Li, R.; Liu, Y.; Wu, S. Particle dynamics and optical appearance of charged spherically symmetric black holes in bumblebee gravity. *Class. Quantum Grav.* **2025**, *42*, 135008. [CrossRef]

Disclaimer/Publisher's Note: The statements, opinions and data contained in all publications are solely those of the individual author(s) and contributor(s) and not of MDPI and/or the editor(s). MDPI and/or the editor(s) disclaim responsibility for any injury to people or property resulting from any ideas, methods, instructions or products referred to in the content.